Article ID: 1000-7032(2023)03-0537-11

Reversible Emission Transformations in Zero-dimensional Hybrid Antimony Chlorides

TAN Li[1], LUO Zhishan[1], LI Qian[2], HAN Jiang[1], ZOU Chao[3], CHANG Xiaoyong[1], QUAN Zewei[1*]

(1. *Department of Chemistry, Southern University of Science and Technology (SUSTech), Shenzhen* 518055, *China*;
2. *Shandong Key Laboratory of Optical Communication Science and Technology, School of Physics Science and Information Technology, Liaocheng University, Liaocheng* 252000, *China*;
3. *Functional Coordination Material Group-Frontier Research Center, Songshan Lake Materials Laboratory, Dongguan* 523808, *China*)
* *Corresponding Author, E-mail: quanzw@sustech.edu.cn*

Abstract: Zero-dimensional (0D) hybrid metal halides with tunable self-trapped exciton (STE) emissions are promising for lighting and displaying applications. In particular, 0D hybrid metal halides with dual-band emissions arising from singlet and triplet STEs have potentials in white-light solid-state lighting. Herein, two 0D hybrid antimony chlorides, $(C_{24}H_{20}P)_2SbCl_5$ (Ⅰ) and $(C_{24}H_{20}P)_2SbCl_5\cdot H_2O\cdot 0.5DMF$ (Ⅱ) ($C_{24}H_{20}P$ = tetraphenylphosphonium, Ph_4P) are reported. The compounds Ⅰ and Ⅱ exhibit single broadband red and yellow emissions upon low-energy (LE) photons (*e.g.* 360 nm) excitation, respectively, arising from their triplet STEs. In addition, upon high-energy (HE) photons (*e.g.* 310 nm) excitation, the compound Ⅱ shows a dual-band emission with an additional blue emission band deriving from singlet STEs, exhibiting a warm-white emission. Intriguingly, a reversible phase transformation between Ⅰ and Ⅱ is achieved through a dynamic insertion and extraction of DMF and water molecules. This work unravels the effect of small molecules on the crystalline structures and the conversion between single- and dual-band emission properties in 0D antimony halides, which could guide the design of 0D hybrid metal halides for sensor applications.

Key words: zero-dimensional; hybrid antimony halide; self-trapped exciton; small molecule; dual-band emission
CLC number: O482.31 **Document code**: A **DOI**: 10.37188/CJL.20220357

基于零维杂化锑基氯化物的可逆荧光发射转化

谭 丽[1], 罗志山[1], 李 茜[2], 韩 江[1], 邹 超[3], 常晓勇[1], 权泽卫[1*]

(1. 南方科技大学 化学系, 广东 深圳 518055;
2. 聊城大学 山东省光通信科学与技术重点实验室, 山东 聊城 252000;
3. 松山湖材料实验室 前沿科学研究-功能配位材料团队, 广东 东莞 523808)

摘要: 零维有机-无机杂化金属卤化物因可调控的自陷态激子发射在发光和显示等领域具有很好的应用前景。特别是同时具有单线态和三线态激子发射双带光谱的零维金属卤化物在白光固态照明应用中极具潜力。本工作报道了两种零维杂化锑基氯化物($(C_{24}H_{20}P)_2SbCl_5$(Ⅰ)和$(C_{24}H_{20}P)_2SbCl_5\cdot H_2O\cdot 0.5DMF$(Ⅱ))($C_{24}H_{20}P$为四苯基膦,$Ph_4P$)。在低能量光子(如360 nm)激发下,化合物Ⅰ和Ⅱ分别呈现出由自陷态激子发射的红色和黄

收稿日期: 2022-09-29; **修订日期**: 2022-10-17
基金项目: 国家自然科学基金(52072166); 广东省自然科学基金(2022A1515010918); 深圳市资助科技创新委员会(KQTD2016-053019134356,RCJC2021060910444106)
Supported by National Natural Science Foundation of China (52072166); Guangdong Science and Technology Department (2022A1515010918); Shenzhen Science and Technology Innovation Committee (KQTD20160530191343 56, RCJC20210609-10444106)

色的单峰宽带光谱。此外，当用高能量光子（如 310 nm）激发时，Ⅱ的光谱呈现出双带白光发射，除黄光发射带外，还出现了一个源于单线态自陷激发发射的蓝光发射带。研究表明，通过引入和去除 DMF 和水分子，化合物Ⅰ和Ⅱ能实现可逆转化。该研究揭示了小分子对零维杂化金属卤化物晶体结构的调控机制，从而实现单带发射和双带发射之间的转变，为设计具有小分子传感应用的零维金属卤化物奠定了研究基础。

关 键 词：零维；杂化锑基氯化物；自陷态激子；小分子；双带发射

1 Introduction

Organic-inorganic hybrid metal halides (HMHs) have attracted increasing research interests due to their wide range of applications in optoelectronic devices, such as light-emitting diodes (LEDs)[1-3], photodetectors[4-6], lasers[7-8] and photovoltaics[9-11]. Based on the spatial arrangement of ionic metal-halide polyhedral building blocks and the surrounding organic cation species, HMHs can be classified into three- (3D), two- (2D), one- (1D) and zero-dimensional (0D) materials. In 0D HMHs, the individual inorganic metal halide polyhedra are completely isolated and surrounded by bulky organic cations to assemble unique host-guest systems. These light-emitting metal halide building blocks periodically embed into the wide bandgap organic cation matrix in 0D HMHs, and then excitons tend to be confined in the individual metal halide polyhedra upon photoexcitation, which facilitates the formation of self-trapped excitons (STEs). In general, the STE emission features strongly Stokes shifted broadband photoluminescence (PL), high photoluminescence quantum yields (PLQYs)[12-13].

Dual-band emission composed of a broad low-energy (LE) band originating from STEs and an additional narrow high-energy (HE) band from free excitons (FEs) have been reported in 2D and 1D HMHs, which makes it easier to achieve a broad white-light emission[14-16]. However, FE emission is rarely observed in 0D HMHs due to the strong exciton confinement effect. Therefore, most of 0D HMHs exhibit only single LE emission band, which limits the formation of dual-band emission to achieve the white-light emission[17]. Recently, dual-band emissions have been reported in 0D Sb-based metal halide $(TTA)_2SbCl_5$ (TTA=tetraethylammonium) and $(TEBA)_2SbCl_5$ (TEBA=benzyltriethylammonium), where the LE emission band covering the orange/yellow spectral range and an additional HE emission band covering the blue spectral range were observed upon HE photons (*e. g.*, 300 nm) excitation, exhibiting ultra-broad white-light emissions. The dual-band emission has been assigned to the singlet and triplet STE emissions[18]. Compared with triplet STE emission, where the strongly Stokes shift broadband emission has a long lifetime (*e. g.*, tens or hundreds of microseconds), singlet STE emission shows a relatively narrow emission band with a fast decay process (*e. g.*, nanoseconds). The dual-band emission in 0D HMHs exhibits potential applications in white-light solid-state lighting[19-20].

On the other hand, the PL emissions in 0D HMHs arising from individual metal halide building blocks are susceptible to the surrounding environments. Solvent molecules are one of the most facile strategies to influence the PL properties in 0D HMHs. The small molecules could insert into the crystalline lattices during crystallization, which affects the interaction between metal halides[21]. For example, the PLQY of $(C_6N_2H_{16})SbCl_5\cdot H_2O$ realized obvious enhancement by incorporation of water molecules into $(C_6N_2H_{16})SbCl_5$, which was ascribed to the formation of more localized photoelectrons resulted from the increased distance between polyhedra[22]. However, the PL switching mechanisms of small molecules on the single- and dual-band emissions in 0D HMHs are still unclear. It is of significance to develop 0D HMHs with tunable white-light emissions and uncover the underlying structure-PL relationships.

In this work, we prepare two eco-friendly 0D antimony (Ⅲ)-based HMHs, $(Ph_4P)_2SbCl_5$ (Ⅰ) and $(Ph_4P)_2SbCl_5\cdot H_2O\cdot 0.5DMF$ (Ⅱ) by carefully control

of the synthesis condition, where a fast crystallization process yields compound Ⅰ, and a slow process favors the formation of solvate Ⅱ. The compound Ⅰ exhibits a red emission centered at 695 nm with a large Stokes shift of 332 nm, and Ⅱ shows a yellow emission peaked at 615 nm with a Stokes shift of 250 nm upon LE photos excitation, originating from triplet STEs. Moreover, Ⅱ shows a dual-band warm white light emission with an additional HE emission band peaked at 470 nm upon HE photos excitation, which is assigned to the singlet STE emission, while Ⅰ remains a single broadband emission. The investigation of temperature-dependent PL properties suggests that the disappearance of singlet STE emission in Ⅰ at room temperature is ascribed to the significantly thermal quenching. Interestingly, the reversible structure and PL conversion between Ⅰ and Ⅱ are achieved, further revealing a dynamic insertion and extraction of DMF and H_2O molecules during the transformation.

2 Experiment

2.1 Materials

Antimony(Ⅲ) chloride($SbCl_3$, 99%) was purchased from Alfa Aesar. Tetraphenylphosphonium chloride(Ph_4PCl, 98%) was obtained from Energy Chemical. N,N-dimethylformamide(DMF, ≥99.5%) was purchased from Shanghai Lingfeng Chemical Reagent. Ethyl acetate(≥99.5%) was purchased from Xilong Scientific. $SbCl_3$ was stored in an air-free, Ar-filled glovebox with O_2 and H_2O level <0.5×10^{-6} (0.5 ppm). And all chemicals were used as received without any further purification.

2.2 Synthesis of $(Ph_4P)_2SbCl_5$(Ⅰ) and $(Ph_4P)_2SbCl_5\cdot H_2O\cdot 0.5DMF$(Ⅱ) Single Crystals

Firstly, 0.27 mmol of $SbCl_3$ and 0.54 mmol of Ph_4PCl were mixed and dissolved in 1 mL of DMF to form a clear precursor solution. Single crystals of Ⅰ were prepared by adding a few drops of ethyl acetate into the precursor solution. Then bulk crystals were prepared by diffusing ethyl acetate into the precursor solution at room temperature. The crystals were then collected and stored in air. Single crystals of Ⅱ were prepared by directly and slowly diffusing ethyl acetate into the precursor solution. The crystals were then collected and stored in air.

2.3 Characterizations

Single crystal X-ray diffraction(SCXRD) data were collected on a Bruker D8 Venture X-ray single crystal diffractometer. Data were measured using monochromatic Mo-Kα radiation at 100 K. Data reduction, scaling and absorption corrections were performed using SAINT(Bruker, V8.38A, 2013). The data were solved by the ShelXT(Sheldrick, 2015) structure solution program using the Intrinsic Phasing solution method and by using Olex2 as the graphical interface[23-24]. The model was refined with version 2016/6 of ShelXL(Sheldrick, 2008) using Least Squares minimization. PXRD patterns were recorded on an X-ray diffractometer(Rigaku SmartLab) with Cu Kα radiation(λ=0.154 18 nm) at a voltage of 45 kV and a current of 200 mA. *In situ* PXRD patterns with the temperature ranging from 25−100 ℃ were performed on a PTC-EVO instrument with a temperature controller. Crystals were grounded into powder followed by filling in a Pt sample holder. Diffraction data were collected with every 10 ℃ increase in temperature. Differential scanning calorimetry(DSC) studies on powder samples were performed with the temperature range from 30 ℃ to 120 ℃ at a rate of 5 ℃·min^{-1} in both heating and cooling runs. Thermogravimetry analyses(TGA) were carried out using a Mettler Toledo instruments with STARe system. The samples were heated from room temperature(~25 ℃) to 800 ℃ at a rate of 10 ℃·min^{-1}, under an argon flux of 30 mL·min^{-1}. The UV-Vis absorption spectra were measured by using a Teflon-lined integrating sphere accessory into Agilent Technologies Cary Series UV-Vis-NIR Spectrophotometer in the range of 200−800 nm. The Photoluminescence(PL) and PL excitation(PLE) spectra were taken by HORIBA Scientific FluoroMax-4 Spectrofluorometer. PL lifetime measurements were performed by Hamamatsu compact fluorescence lifetime spectrometer C11367. The PL decay curves of Ⅰ and Ⅱ were fitted by using U11487 Software from Hamamatsu Photonics at room temperature, and the average radiative lifetime was determined by monoexponetial

fitting. The absolute PLQYs were recorded with Hamamatsu spectrometer C11347.

3 Results and Discussion

The crystalline structures of Ⅰ and Ⅱ are determined by single crystal X-ray diffraction (SCXRD). Although both compounds possess the same triclinic space group $P\bar{1}$, the crystallographic data are different(Tab. S1). For example, Ⅰ has cell parameters of a=0.999 10(7) nm, b=1.001 99(7) nm, c=1.214 52(8) nm, and α = 99.366(2)°, β = 94.602(2)°, γ = 113.731(2)°, V= 1.083 81(13) nm^3. While Ⅱ possesses the cell dimensions of a =1.196 49(5) nm, b = 1.269 46(5) nm, c = 1.269 46(5) nm, and α = 100.749 0(10)°, β = 110.924 0(10)°, γ = 90.228 0(10)°, V = 2.312 13(17) nm^3. The crystalline structures of Ⅰ and Ⅱ are shown in Fig. 1(a) and (c), with individual $[SbCl_5]^{2-}$ pyramids surrounded by bulky Ph_4P^+ cations. The obvious structural difference between Ⅰ and Ⅱ is that DMF and water molecules are present in the single crystal of Ⅱ. Considering that compound Ⅱ was obtained *via* a relatively slow diffusion process by using a less volatile solvent as the antisolvent, which allows the solvent molecules(*i. e.*, DMF, H_2O) to enter into the crystalline lattices during the crystallization (Fig. 1(c)). In addition, hydrogen bonds of C—H···Cl and C—H···O can be found in compound Ⅱ. The incorporation of DMF and H_2O molecules could induce the reorganization of the organic cations and inorganic polyhedra, resulting in a smaller distance between the neighboring square pyramids and a longer vertical Sb—Cl bond in the pyramidal unit. As shown in Fig. 1(b) and (d), the smallest distance between $[SbCl_5]^{2-}$ units decreases from 0.999 nm for Ⅰ to 0.793 nm for Ⅱ, and the vertical Sb—Cl bond length increases from 0.220 nm in Ⅰ to 0.239 nm in Ⅱ. In addition, the calculated distortion indexes (D_{dis}, calculated by equation S1, see the details in Supporting Information) of the $[SbCl_5]^{2-}$ in compounds

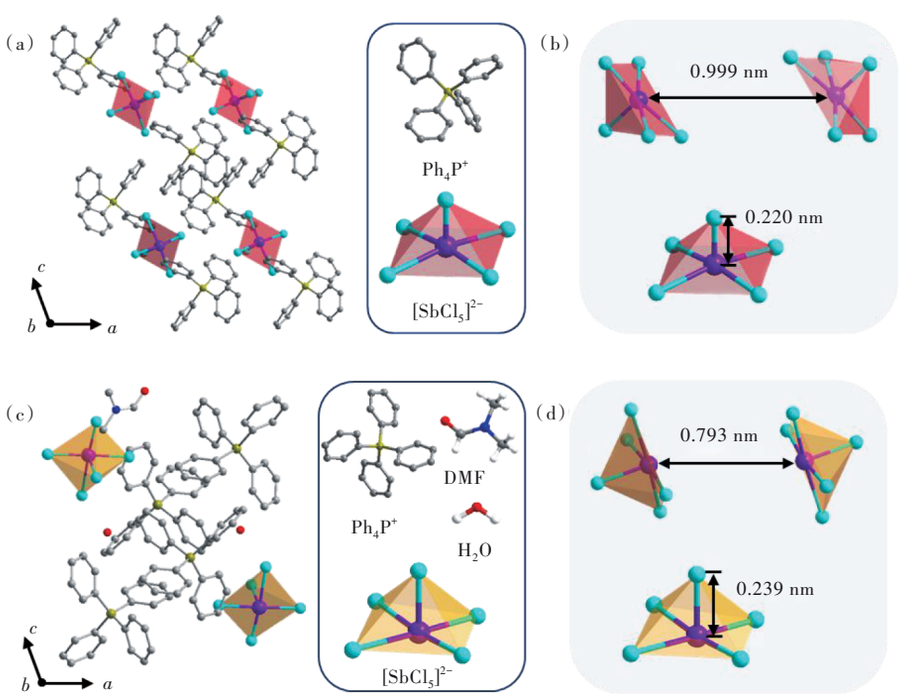

Fig.1 (a) Crystal structure of Ⅰ and the corresponding building blocks of Ph_4P^+ and $[SbCl_5]^{2-}$. (b) The smallest distance between two neighboring pyramids and the vertical Sb—Cl bond in pyramidal unit in compound Ⅰ. (c) Crystal structure of $(Ph_4P)_2SbCl_5\cdot H_2O\cdot 0.5DMF$(Ⅱ) and the corresponding building blocks of Ph_4P^+ and $[SbCl_5]^{2-}$ as well as DMF and water molecule. Purple spheres: Sb atoms; cyan spheres: Cl atoms; yellow spheres: Br atoms; grey spheres: C atoms; dark yellow spheres: P atoms; blue spheres: N atoms; red spheres: O atoms; white spheres: H atoms, red and yellow pyramids: $[SbCl_5]^{2-}$ species. (d) The smallest distance between two neighboring pyramids and the vertical Sb—Cl bond in pyramidal unit in compound Ⅱ.

Ⅰ and Ⅱ are 0.004 632 and 0.004 611, respectively, which are similar to those of the reported 0D hybrid antimony halides[25-26]. It is expected that the slightly larger structural distortions in compound Ⅰ may result in larger Stokes shifts and broader emissions than those of compound Ⅱ. The phase purities of Ⅰ and Ⅱ are confirmed by powder X-ray diffraction (PXRD) measurements (Fig. S1 and S2). TGA measurements of the fresh samples of Ⅰ and Ⅱ are shown in Fig. S3, a weight loss of 6% in Ⅱ below 200 ℃ is monitored, corresponding to the evaporation of DMF and H_2O molecules. In contrast, there is little weight loss in Ⅰ until up to 300 ℃.

The optical properties of Ⅰ and Ⅱ are characterized by UV-Vis absorption, steady-state and time-resolved PL emissions. As shown in Fig. 2, the PL excitation (PLE) spectra of both samples show wide bands covering the range of 250–450 nm, in agreement with the absorption spectra (Fig. S4). The PLE and emission spectra show that the PL peak for Ⅰ locates at 695 nm with a large Stokes shift of 332 nm and a full width at half-maximum (FWHM) of 175 nm (0.447 eV) upon 363 nm excitation (Fig. 2(a)). The emission in compound Ⅱ peaked at 615 nm has a Stokes shift of 250 nm with a FWHM of 150 nm (0.465 eV) upon 360 nm excitation (Fig. 2(d)). Compared with Ⅱ, compound Ⅰ displays a redshifted PL emission, broader FWHM and larger Stokes shift, indicating a greater excited state structural distortion. It has been reported that the structural distortion during the excitation relaxation involves the elongation of the vertical Sb—Cl bond[17]. Therefore, the increased Stokes shift in Ⅰ could be ascribed to its shorter vertical Sb—Cl bond in $[SbCl_5]^{2-}$ pyramid than that of Ⅱ, which undergoes a stronger excited state distortion. Moreover, a larger distance between the neighboring polyhedra allows a greater structural distortion in Ⅰ[27-28]. The photographs of Ⅰ and Ⅱ single crystals under natural light and 365 nm UV light are shown in Fig. 2(b) and (e), respectively. Both crystals are clear and transparent under natural light. However, under 365 nm ultraviolet light Ⅰ and Ⅱ exhibit bright red and yellow emissions, respectively. The Commission Internationale de l'

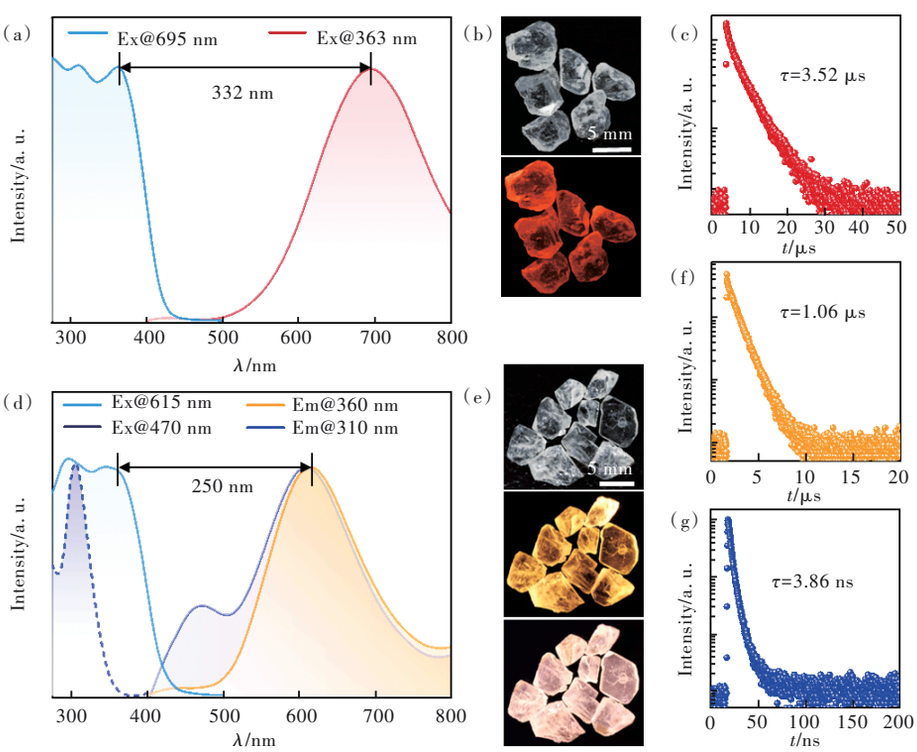

Fig.2　(a) Excitation and emission spectra of Ⅰ. (b) Single crystals of Ⅰ under natural light and 365 nm UV light. (c) Time-resolved PL decay curve of Ⅰ upon 360 nm excitation. (d) Excitation and emission spectra of Ⅱ. (e) Single crystals of Ⅱ under natural light, 365 nm and 302 nm UV light. (f) Time-resolved PL decay curve of Ⅱ at room temperature upon 360 nm excitation. (g) Time-resolved PL decay curve of Ⅱ under 310 nm excitation.

Eclairage(CIE) chromaticity coordinates for Ⅰ and Ⅱ are (0.60, 0.38) and (0.54, 0.44) upon 360 nm excitation, respectively (Fig. S5). The PLQY of Ⅰ is measured as 49%, which is higher than that of Ⅱ (14%). The decreased PLQY in Ⅱ could be resulted from the reduced distance between the neighboring polyhedra upon incorporation of solvent molecules(Fig. 1(b) and (d)). The time-resolved PL of Ⅰ and Ⅱ exhibit monoexponential decays with the individual lifetime of 3.52 μs and 1.06 μs, respectively(Fig. 2(c) and (f)). The main optical properties of Ⅰ and Ⅱ are summarized in Tab. S2.

The characteristics of broad FWHMs, large Stokes shifts and long PL decay lifetime of both compounds suggest that the PL emission of Ⅰ centered at 695 nm and Ⅱ peaked at 615 nm are derived from triplet STE emission from $[SbCl_5]^{2-}$ units. The origin of the PL emissions is further confirmed by the power density-dependent PL intensity, which exhibits a linear relationship, excluding the effect of permanent defects (Fig. S6)[22,29]. Note that the PL spectra of Ⅰ exhibit identical shapes and features with the excitation wavelengths ranging from 280 nm to 360 nm(Fig. S7). However, the PL emission in Ⅱ exhibits a dual-band emission with an additional HE band peaked at 470 nm upon HE photons excitation (Fig. 2(d) and S8). The excitation spectrum of Ⅱ monitored at HE emission maximum shows a sharp peak at around 310 nm, revealing another emission center(Fig. 2(d)). The PL decay lifetime monitored at 470 nm is about 3.86 ns(Fig. 2(g)), which is quite different from that of the organic molecule Ph_4PCl (millisecond-level)[30]. Therefore, the HE emission centered at 470 nm should not originate from the organic component, but rather from the singlet STEs[18].

It is noteworthy that the dual-band emission in compound Ⅱ gives rise to a warm white-light emission, having a CIE chromaticity coordinate of (0.44, 0.39) upon HE photons excitation (Fig. 2(e) and S5). The appearance of HE band in a dual-band emission facilitates the PL tunability in a wide range, producing the white-light emission. The "static" $5S^2$ lone pair in Sb^{3+} is expressed in coordinatively unsaturated geometries (*e. g.*, square pyramids $[SbX_5]^{2-}$), which reduces symmetry imposed by these motifs and has the singlet electronic ground state ($^1S_0$). The non-degenerate excited states will split into one singlet state $^1P_1$ and three triplet states ^3P_n (n=0, 1, 2)[19, 31-32]. Therefore, the dual-band emission in compound Ⅱ can be attributed to the transitions of $^3P_1 \rightarrow {}^1S_0$ and $^1P_1 \rightarrow {}^1S_0$, which correspondingly generate the singlet and triplet exciton emissions in compound Ⅱ.

To gain a deep insight into the PL properties of compounds Ⅰ and Ⅱ and further examine the underlying reason for the absence of HE emission in compound Ⅰ at room temperature, temperature-dependent emission spectra are investigated in both compounds. For compound Ⅰ, upon 360 nm excitation, a new emission band peaked at 605 nm appears besides the emission band centered at 695 nm as the temperature drops from room temperature to 78 K (Fig. S9 and S10). The lifetime of the dual-band emission centered at 605 nm and 695 nm is measured to be 2.83 μs and 7.24 μs at 78 K, respectively, suggesting the presence of two triplet emission states(Fig. S11). Such a PL emission transition with temperature may be attributed to the increased rigidity of molecular environment and reduced thermal energy with decreasing temperature[33]. Upon 310 nm excitation, another additional HE emission peaked at 440 nm in compound Ⅰ appears and gradually intensifies upon cooling the sample to 78 K (Fig. 3(a)). The PLE spectrum monitored at 440 nm shows a sharp peak of 310 nm with the measured lifetime of 7.61 ns at 78 K, suggesting the singlet STE emission nature(Fig. S10 and S11). However, the HE emission disappears above 180 K(Fig. 3(a) and S9(b)). For compound Ⅱ, the PL intensity of the emission centered at 615 nm gradually increases when the temperature decreases to 78 K under the excitation wavelength of 360 nm(Fig. S9(c)). Upon 310 nm excitation, the intensities of the dual-band emission peaked at 470 nm and 615 nm gradually increase with the temperature dropping from room temperature to 78 K(Fig. 3(b)). The PL decay lifetime is measured to be 13.11 ns and 3.98 μs at 78 K,

corresponding to the singlet and triplet STE emissions, respectively (Fig. S12 and S13). Therefore, the photophysical process can be illustrated in Fig. 3(c). The ground state of Sb^{3+} is $^1S_0$, and excited state of Sb^{3+} has four levels, $^3P_0$, $^1P_1$, $^3P_2$ and $^3P_1$[34]. At room temperature, the electrons of compound Ⅰ in ground states are excited to the excited states $^3P_1$, then the excitons undergo a self-trapped process with triplet STEs caused by highly distorted $[SbCl_5]^{2-}$ pyramids under photoexcitation. The radiative transition from the triplet STEs gives rise to the largely Stokes-shifted broadband emission. In compound Ⅱ, the electrons can be excited to the excited states $^1P_1$ and $^3P_1$ upon HE photos (*e. g.*, 310 nm) excitation, then the excitons get self-trapped with singlet STEs and triplet STEs. Thus, a dual-band emission with fluorescent emission and phosphorescent emission is observed upon the radiative transition of these two types of STEs. While only triplet STEs exist upon LE photos (*e. g.*, 360 nm) excitation, resulting in a single LE broadband emission. At low temperature (*e. g.*, 78 K), both compounds exhibit HE and LE band emissions originating from singlet STEs and triplet STEs upon HE photos excitation, however, the HE emission band disappears in compound Ⅰ above 180 K.

To explain the disappearance of HE emission with temperature in compound Ⅰ upon HE photons excitation, the thermal evolution of the integrated PL intensity of both compounds upon 310 nm excitation is analyzed. The thermal quenching model adopts the Shibata model[35], which involves two competing thermal dissociation processes of the singlet exciton and triplet exciton. Therefore, the thermal quenching can be described by the following formula[36]

$$I(T) = I_0 \frac{1 + c \times \exp\left(-\frac{E_c}{k_B T}\right)}{1 + a \times \exp\left(-\frac{E_a}{k_B T}\right) + b \times \exp\left(-\frac{E_b}{k_B T}\right)}, \quad (1)$$

where I_0 is the low-temperature PL intensity, E_a is the self-trapped depth, E_b is the activation energy associated with the exciton binding energy, E_c describes the thermal quenching of the PL intensity, and a, b and c are fitting parameters. The fitting results give E_a = 579 meV, E_b = 267 meV and E_c = 185 meV for compound Ⅰ and E_a = 784 meV, E_b = 159 meV, and E_c = 7 meV for Ⅱ (Fig. 3(d) and 3(e)). Note that the obtained E_c values for Ⅰ is much larger than that of Ⅱ, suggesting a stronger

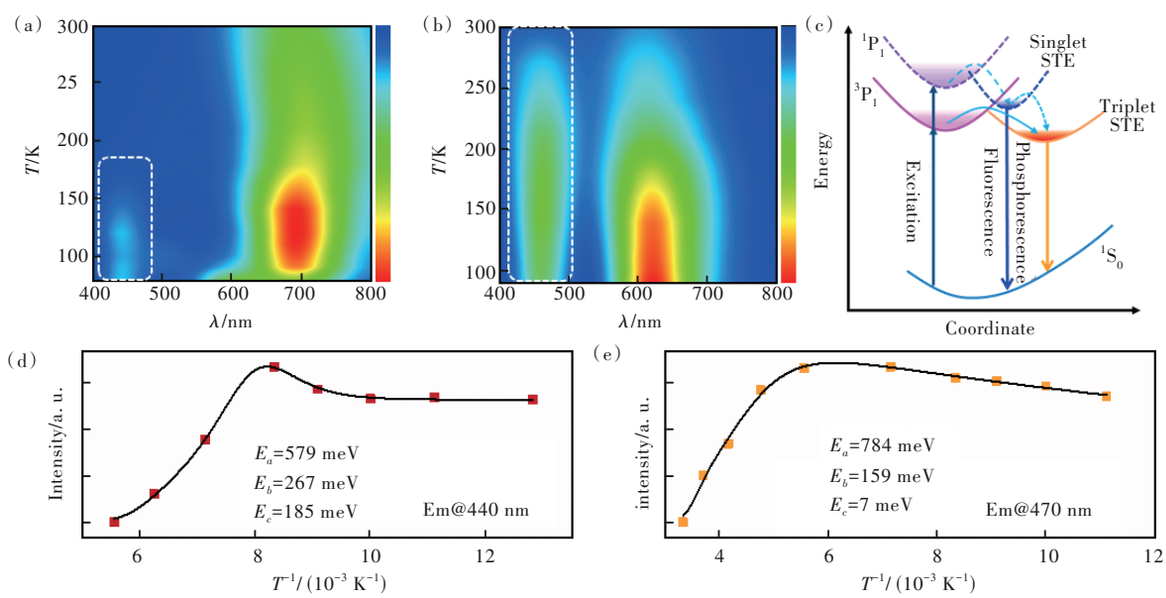

Fig.3　(a) Temperature-dependent emission spectra of Ⅰ upon 310 nm excitation. (b) Temperature-dependent emission spectra of Ⅱ under 310 nm excitation. (c) Coordinate diagram illustrating the photophysical process of $[SbCl_5]^{2-}$ pyramids in Ⅰ and Ⅱ. (d) Thermal evolution of integrated PL intensity of Ⅰ with the emission centered at 440 nm upon 310 nm excitation. (e) Thermal evolution of integrated PL intensity of Ⅱ with the emission centered at 470 nm upon 310 nm excitation.

thermal quenching effect through non-radiative recombination(NR) in Ⅰ. Therefore, the singlet STE emission in Ⅰ is not observed at room temperature, and a dual-band warm-white emission could be achieved in Ⅱ upon HE photos excitation.

Remarkably, the exposure of Ⅰ crystals to residual DMF and moisture for a few days, the red emission is gradually converted into a yellow emission under UV light illumination. As shown in Fig. 4, the optical properties of the fully converted products from Ⅰ are almost identical to those of compound Ⅱ, exhibiting triplet STE emissions under LE photons excitation and dual-band emissions upon HE photons excitation (Fig. S14). Furthermore, SCXRD characterizations of the converted crystals show the same space group and similar crystallographic data as Ⅱ, confirming the successful transformation(Tab. S1). In addition, the phase purity of the converted compound is also confirmed by PXRD pattern (Fig. S15). Given that compound Ⅱ was obtained *via* a relatively slow crystal growth process, which would facilitate the participation of solvent molecules (*i. e.* DMF, H_2O) in the crystallization. Therefore, the exposure of Ⅰ to the residual DMF and moisture allows the entrance of the solvent molecules into crystalline lattices, leading to the phase transformation from Ⅰ to Ⅱ. However, such conversion could be suppressed by removal of either DMF or water solvent, verifying the cooperative effects of DMF and moisture on this conversion.

Generally, if the phase transition is induced by solvent molecules, a reversible phase transformation could occur by removal of solvent molecules *via* thermal treatment. As expected, the excitation and PL emission spectra of the converted products from Ⅱ after thermal treatment are similar to those of Ⅰ (Fig. 4(b) and S16). Moreover, the PXRD characterization shows that the obtained product possesses

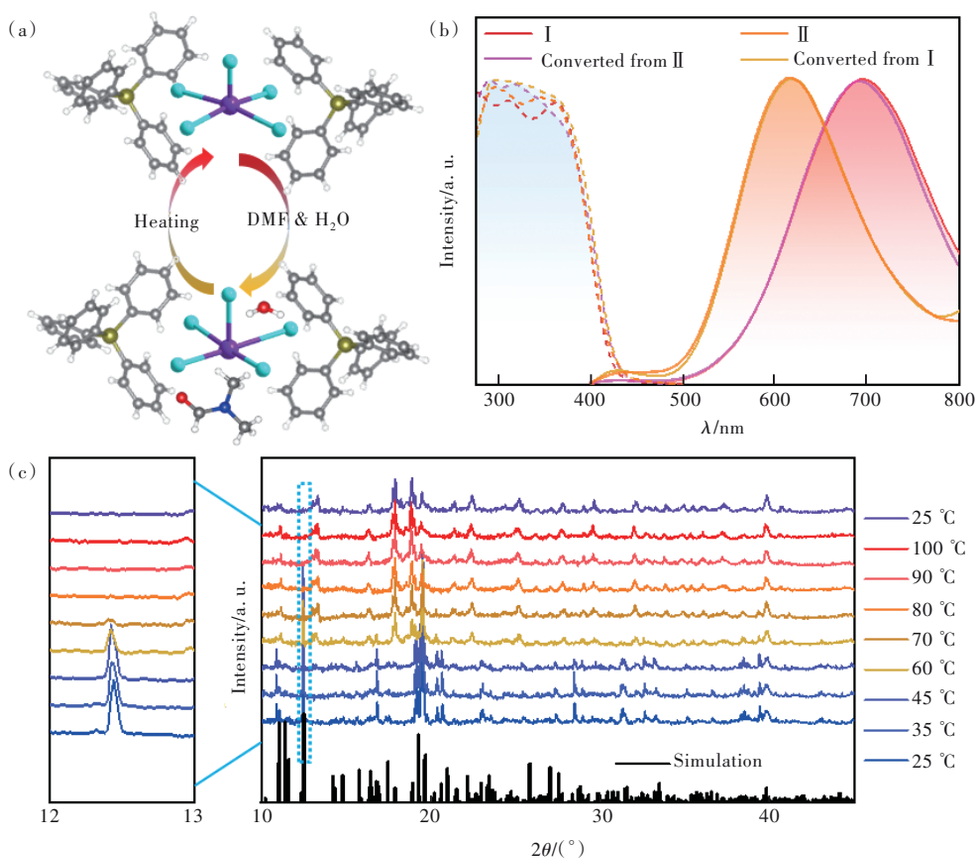

Fig.4 (a)Illustration of the transformation between Ⅰ and Ⅱ. (b)Excitation and emission spectra of Ⅰ and Ⅱ, as well as compounds converted from Ⅰ and Ⅱ. (c)*In situ* PXRD patterns of Ⅱ upon thermal treatment from 25 ℃ to 100 ℃, then cooled to 25 ℃. The enlarged-view of PXRD patterns with 2θ between 12° and 13° are shown on the left.

the same phase as Ⅰ (Fig. S17). Although we fail to obtain the high quality diffraction data to solve the crystal structure by *in situ* SCXRD characterization due to the formation of an opaque surface under heating (Fig. S18), *in situ* temperature-dependent PXRD measurements are performed to monitor the conversion process. The PXRD patterns exhibit that the peak at 12.4° gradually vanished while a peak at 13.2° increased with temperature, confirming the phase transformation from Ⅱ to Ⅰ with the conversion temperature lying between 70–80 ℃(Fig. 4(c)). To further study the thermal induced phase transition, the differential scanning calorimetry (DSC) traces for both heating and cooling runs of Ⅱ are shown in Fig. S19. The heating scan shows an endothermic transition at around 75 ℃, in good agreement with *in situ* PXRD measurements. It has been reported that small molecules in solution could affect the electronic spectra, and thus, the transformation of the structures and PL emissions between Ⅰ and Ⅱ can be ascribed to the dynamic insertion and removal of solvent molecules of the crystals[21].

4　Conclusion

In summary, two environment-friendly 0D HMHs of $(Ph_4P)_2SbCl_5$ (Ⅰ) and $(Ph_4P)_2SbCl_5 \cdot H_2O \cdot 0.5DMF$ (Ⅱ) have been prepared through antisolvent diffusion-dependent crystallization. Upon LE photons excitation, Ⅰ and Ⅱ exhibit strongly Stokes shifted broadband red and yellow PL emissions, respectively, originating from triplet STEs. While upon HE photons excitation, Ⅱ shows a dual-band warm white-light emission with an additional HE band (*i. e.*, blue emission) arising from singlet STEs. The disappearance of HE band in Ⅰ is ascribed to the significantly thermal quenching at room temperature. Interestingly, the reversible heat-solvent induced structure and PL transformations between Ⅰ and Ⅱ are achieved. Our results provide two generally efficient strategies (synthesis and post-synthesis) to design materials with switchable PL properties between the single- and dual-band emission in 0D Sb-based HMHs. The modulation mechanism of dynamic incorporation/removal of solvent molecules in this work enables further exploration of novel functional materials for diverse applications, such as small molecule sensors.

Supplementary Information and Response Letter are available for this paper at: http://cjl.lightpublishing.cn/thesisDetails#10.37188/CJL.20220357.

References:

[1] LIN K B, XING J, QUAN L N, *et al.* Perovskite light-emitting diodes with external quantum efficiency exceeding 20 per cent [J]. *Nature*, 2018, 562(7726): 245-248.

[2] ZHAO X F, TAN Z K. Large-area near-infrared perovskite light-emitting diodes [J]. *Nat. Photonics*, 2020, 14(4): 215-218.

[3] FAKHARUDDIN A, GANGISHETTY M K, ABDI-JALEBI M, *et al.* Perovskite light-emitting diodes [J]. *Nat. Electron.*, 2022, 5(4): 203-216.

[4] ZHAO Y X, ZHU K. Organic-inorganic hybrid lead halide perovskites for optoelectronic and electronic applications [J]. *Chem. Soc. Rev.*, 2016, 45(3): 655-689.

[5] GAN Z X, CHENG Y C, CHEN W J, *et al.* Photophysics of 2D organic-inorganic hybrid lead halide perovskites: progress, debates, and challenges [J]. *Adv. Sci.*, 2021, 8(6): 2001843-1-18.

[6] LEUNG S F, HO K T, KUNG P K, *et al.* A self-powered and flexible organometallic halide perovskite photodetector with very high detectivity [J]. *Adv. Mater.*, 2018, 30(8): 1704611-1-8.

[7] ZHU H M, FU Y P, MENG F, *et al.* Lead halide perovskite nanowire lasers with low lasing thresholds and high quality factors [J]. *Nat. Mater.*, 2015, 14(6): 636-642.

[8] ZHANG H H, LIAO Q, WU Y S, *et al.* 2D Ruddlesden-Popper perovskites microring laser array [J]. *Adv. Mater.*, 2018, 30(15): 1706186-1-8.

[9] LI Z, KLEIN T R, KIM D H, *et al*. Scalable fabrication of perovskite solar cells [J]. *Nat. Rev. Mater.*, 2018, 3(4): 18017-1-20.

[10] CORREA-BAENA J P, SALIBA M, BUONASSISI T, *et al*. Promises and challenges of perovskite solar cells [J]. *Science*, 2017, 358(6364): 739-744.

[11] ZHAO Y, MA F, QU Z H, *et al*. Inactive $(PbI_2)_2RbCl$ stabilizes perovskite films for efficient solar cells [J]. *Science*, 2022, 377(6605): 531-534.

[12] ZHOU C K, LIN H R, TIAN Y, *et al*. Luminescent zero-dimensional organic metal halide hybrids with near-unity quantum efficiency [J]. *Chem. Sci.*, 2018, 9(3): 586-593.

[13] LUO Z S, LIU Y J, LIU Y L, *et al*. Integrated afterglow and self-trapped exciton emissions in hybrid metal halides for anti-counterfeiting applications [J]. *Adv. Mater.*, 2022, 34(18): 2200607-1-8.

[14] DOHNER E R, HOKE E T, KARUNADASA H I. Self-assembly of broadband white-light emitters [J]. *J. Am. Chem. Soc.*, 2014, 136(5): 1718-1721.

[15] WANG X M, MENG W W, LIAO W Q, *et al*. Atomistic mechanism of broadband emission in metal halide perovskites [J]. *J. Phys. Chem. Lett.*, 2019, 10(3): 501-506.

[16] HU T, SMITH M D, DOHNER E R, *et al*. Mechanism for broadband white-light emission from two-dimensional (110) hybrid perovskites [J]. *J. Phys. Chem. Lett.*, 2016, 7(12): 2258-2263.

[17] ZHOU C K, WORKU M, NEU J, *et al*. Facile preparation of light emitting organic metal halide crystals with near-unity quantum efficiency [J]. *Chem. Mater.*, 2018, 30(7): 2374-2378.

[18] LI Z Y, LI Y, LIANG P, *et al*. Dual-band luminescent lead-free antimony chloride halides with near-unity photoluminescence quantum efficiency [J]. *Chem. Mater.*, 2019, 31(22): 9363-9371.

[19] JING Y Y, LIU Y, LI M Z, *et al*. Photoluminescence of singlet/triplet self-trapped excitons in Sb^{3+}-based metal halides [J]. *Adv. Opt. Mater.*, 2021, 9(8): 2002213-1-15.

[20] LI C, LUO Z S, LIU Y L, *et al*. Self-trapped exciton emission with high thermal stability in antimony-doped hybrid manganese chloride [J]. *Adv. Opt. Mater.*, 2022, 10(12): 2102746.

[21] LUO J B, WEI J H, ZHANG Z Z, *et al*. Water-molecule-induced emission transformation of zero-dimension antimony-based metal halide [J]. *Inorg. Chem.*, 2022, 61(1): 338-345.

[22] SONG G M, LI M Z, ZHANG S Z, *et al*. Enhancing photoluminescence quantum yield in 0d metal halides by introducing water molecules [J]. *Adv. Funct. Mater.*, 2020, 30(32): 2002468-1-6.

[23] DOLOMANOV O V, BOURHIS L J, GILDEA R J, *et al*. OLEX2: a complete structure solution, refinement and analysis program [J]. *J. Appl. Crystallogr.*, 2009, 42(2): 339-341.

[24] SHELDRICK G M. SHELXT—Integrated space-group and crystal-structure determination [J]. *Acta Crystallogr.*, 2015, 71A(1): 3-8.

[25] SU B B, GENG S N, XIAO Z W, *et al*. Highly distorted antimony(Ⅲ) chloride $[Sb_2Cl_8]^{2-}$ dimers for near-infrared luminescence up to 1 070 nm [J]. *Angew. Chem. Int. Ed.*, 2022, 61(33): e202208881-1-5.

[26] WANG Z P, XIE D L, ZHANG F, *et al*. Controlling information duration on rewritable luminescent paper based on hybrid antimony (Ⅲ) chloride/small-molecule absorbates [J]. *Sci. Adv.*, 2020, 6(48): eabc2181-1-9.

[27] BENIN B M, DIRIN D N, MORAD V, *et al*. Highly emissive self-trapped excitons in fully inorganic zero-dimensional tin halides [J]. *Angew. Chem. Int. Ed.*, 2018, 57(35): 11329-11333.

[28] SHI H L, HAN D, CHEN S Y, *et al*. Impact of metal ns^2 lone pair on luminescence quantum efficiency in low-dimensional halide perovskites [J]. *Phys. Rev. Mater.*, 2019, 3(3): 034604-1-7.

[29] LUO J J, WANG X M, LI S R, *et al*. Efficient and stable emission of warm-white light from lead-free halide double perovskites [J]. *Nature*, 2018, 563(7732): 541-545.

[30] CHEN G L, ZHOU J, FENG H, *et al*. A simple and efficient phosphorescent probe for iodide-specific detection based on crystallization-induced phosphorescence of organic ionic crystals [J]. *J. Mater. Chem.* C, 2019, 7(1): 43-47.

[31] MCCALL K M, MORAD V, BENIN B M, *et al*. Efficient lone-pair-driven luminescence: structure-property relationships in emissive $5s^2$ metal halides [J]. *ACS Mater. Lett.*, 2020, 2(9): 1218-1232.

[32] LIU M Z, DUAN C K, TANNER P A, *et al*. Understanding photoluminescence of Cs_2ZrCl_6 doped with post-transition-metal ions using first-principles calculations [J]. *Phys. Rev.* B, 2022, 105(19): 195137.

[33] ZHOU C K, LIN H R, NEU J, *et al.* Green emitting single-crystalline bulk assembly of metal halide clusters with near-unity photoluminescence quantum efficiency [J]. *ACS Energy Lett.*, 2019, 4(7): 1579-1583.

[34] RANFAGNI A, MUGNAI D, BACCI M, *et al.* The optical properties of thallium-like impurities in alkali-halide crystals [J]. *Adv. Phys.*, 1983, 32(6): 823-905.

[35] SHIBATA H. Negative thermal quenching curves in photoluminescence of solids [J]. *Jpn. J. Appl. Phys.*, 1998, 37(2): 550-553.

[36] ROCCANOVA R, YANGUI A, SEO G, *et al.* Bright luminescence from nontoxic $CsCu_2X_3$ (X = Cl, Br, I) [J]. *ACS Mater. Lett.*, 2019, 1(4): 459-465.

谭丽(1988-),女,湖南衡阳人,博士,2018年于德国波茨坦大学获得博士学位,主要从事金属卤化物合成及其光谱性能的研究。

E-mail: tanlijanis@126.com

权泽卫(1982-),男,河南洛阳人,博士,教授,博士生导师,2009年于中国科学院长春应用化学研究所获得博士学位,主要从事新型无机功能材料的研究。

E-mail: quanzw@sustech.edu.cn